Photo-induced changes in tissue stiffness alter epithelial budding morphogenesis in the embryonic lung

Kara E. Peak[1], Poornacharanya Rajaguru[1], Adil Khan[1], Jason P. Gleghorn[2], Girgis Obaid[1], Jacopo Ferruzzi[1,3], Victor D. Varner[1,3,*]

[1]Department of Bioengineering, University of Texas at Dallas, Richardson, TX

[2]Department of Biomedical Engineering, University of Delaware, Newark, DE

[3]Department of Biomedical Engineering, UT Southwestern Medical Center, Dallas, TX

* Address correspondence to V.D.V (vdv@utdallas.edu; victor.varner@utsouthwestern.edu)

Keywords: lung development; biomechanics; fibroblast growth factor-10 (FGF-10); microindentation; computational modeling, Rose Bengal

Abstract

Extracellular matrix (ECM) stiffness has been shown to influence the differentiation of progenitor cells in culture, but a lack of tools to perturb the mechanical properties within intact embryonic organs has made it difficult to determine how changes in tissue stiffness influence organ patterning and morphogenesis. Photocrosslinking of the ECM has been successfully used to stiffen soft tissues, such as the cornea and skin, which are optically accessible, but this technique has not yet been applied to developing embryos. Here, we use photocrosslinking with Rose Bengal (RB) to locally and ectopically stiffen the pulmonary mesenchyme of explanted embryonic lungs cultured *ex vivo*. This change in mechanical properties was sufficient to suppress FGF-10-mediated budding morphogenesis along the embryonic airway, without negatively impacting patterns of cell proliferation or apoptosis. A computational model of airway branching was used to determine that FGF-10-induced buds form via a growth-induced buckling mechanism and that increased mesenchymal stiffness is sufficient to inhibit epithelial buckling. Taken together, our data demonstrate that photocrosslinking can be used to create regional differences in mechanical properties within intact embryonic organs and that these differences influence epithelial morphogenesis and patterning. Further, this photocrosslinking assay can be readily adapted to other developing tissues and model systems.

Introduction

Mechanical inputs, such as forces, deformations, and changes in stiffness, have been shown to influence aspects of embryonic development[1,2]. Time-varying changes in mechanical properties, for instance, are associated with a variety of developmental events, including early embryonic cleavage, notochord elongation, gastrulation, and cardiac looping[3–7]. This work has revealed that differences in mechanics are present at different embryonic stages, but there is little *in vivo* (or *ex vivo*) data demonstrating that altered mechanical properties can directly influence organ patterning and morphogenesis. A variety of *in vitro* assays have been used to show that changes in substratum stiffness can regulate the differentiation of isolated progenitor cells[8], but this idea has yet to be demonstrated within the context of organogenesis, in part owing to a lack of experimental tools to modulate mechanical properties within intact embryonic organs. Recent work has shown that the extracellular matrix (ECM) degradation or patterning can influence branching morphogenesis[9,10], but these changes have not been connected directly to changes in mechanical properties. Here, we present a new technique that uses photocrosslinking to locally modulate tissue stiffness in embryonic lungs cultured *ex vivo* and assess how these mechanical changes influence epithelial budding.

Exposure to light can elicit a variety of specific chemical reactions, which over the years have proved useful for several biomedical applications[11]. Photosensitive synthetic polymers, for instance, have been used to create hydrogel-based biomaterials with tunable mechanical properties for 3D cell and organoid culture[12–14]. In addition, the light-initiated crosslinking of native ECM with specific photo-activatable dyes, such as riboflavin and Rose Bengal (RB), has been used to stiffen collagen gels[15,16], restore mechanical integrity to diseased corneas[17–20], and aid in dermal wound closure[21]. To our knowledge, however, these photocrosslinking assays have never been adapted to the study of embryonic organs, possibly owing to the need for tissues to be

43 optically accessible. RB is activated by the presence of green light (530-560 nm)[22] and can alter
44 ECM crosslinking and mechanical properties within both 3D collagen gels[15] and soft tissues like
45 the cornea and skin[19,21] (Fig. 1A). Here, we capitalized on the biocompatibility of RB and adapted
46 RB-mediated photocrosslinking to the *ex vivo* culture of an explanted embryonic organ, using the
47 developing avian lung as an illustrative example.
48
49 Numerous organs, including the lung, kidney, and salivary gland, form via a process known as
50 branching morphogenesis, wherein a simple epithelial tube undergoes a series of branching
51 events to build a ramified tree[23,24]. In the embryonic lung, airway branching involves distinct
52 branching modes: lateral branches, which emerge along the length of a parent branch, and
53 bifurcations, in which the tip of a parent branch splits[25]. This process is regulated, in part, by
54 reciprocal signaling interactions between the branching airway epithelium and the surrounding
55 layer of pulmonary mesenchyme[26], but branching morphogenesis can also be influenced by
56 changes in mechanics[27–35]. Focal regions of fibroblast growth factor (FGF)-10 expression in the
57 pulmonary mesenchyme are thought to specify the formation of individual buds and provide a
58 biochemical template for the overall branching pattern[36]. However, we have recently shown that
59 individual sources of FGF-10 can promote bud formation via epithelial buckling[37]. In general,
60 buckling morphogenesis can depend on relative differences in mechanical properties between
61 adjacent tissue layers[28,38]; however, previous studies have not yet explored how altered tissue
62 stiffness influences FGF-10-induced budding. Here, we present a new RB photocrosslinking
63 assay to locally and ectopically stiffen the pulmonary mesenchyme of cultured embryonic avian
64 lungs. This technique is then combined with micro-mechanical testing, quantitative fluorescence
65 microscopy, and computational modeling to determine how regional differences in stiffness
66 influence FGF-10-induced budding morphogenesis.

Results

Ectopically stiffening the pulmonary mesenchyme inhibits FGF-10-induced budding morphogenesis

We embedded RB-loaded beads within the pulmonary mesenchyme of explanted embryonic avian lungs, irradiated them with green light (fluence levels of 0, 0.5, or 1 J/cm^2) to promote photocrosslinking of the tissue, and determined how changes in mechanical properties influence FGF-10-mediated budding morphogenesis. In previous work, we showed that individual focal sources of FGF-10 can elicit the formation of multiple supernumerary buds along the primary bronchus of cultured explants[37]. Following irradiation with light, agarose beads loaded with both RB and FGF-10 showed decreased levels of bud formation at increased fluence levels, as compared to either "no light" controls (containing RB) or contralateral controls (containing only FGF-10) (Fig. 1B-E). These data suggested that increased levels of RB-mediated photocrosslinking were suppressing the formation of FGF-10-induced supernumerary buds. (Higher fluence levels ($\geq$ 2 J/cm^2) compromised the viability of the cultured explants (Supplementary Fig.1)). Morphometric analysis of epithelial geometry further highlighted these differences. Treatment with FGF-10 alone elicited an increase in both epithelial length and tortuosity, which coincided with the emergence of new epithelial buds (Fig. 1E-G); however, RB-mediated photocrosslinking (at 1 J/cm^2) produced a less elongated and less tortuous epithelium with fewer FGF-10-induced buds as compared to both "no light" and contralateral controls (Fig. 1F-G).

To confirm that photocrosslinking with RB produced a change in tissue stiffness, we used our customized microindentation system to quantify regional differences in the mechanical properties of the pulmonary mesenchyme (Fig. 1H; Supplementary Fig. 2). Irradiated lungs exhibited a fluence-dependent increase in mesenchymal stiffness, wherein the lobes containing an RB-

92 loaded bead were significantly stiffer than either “no light” or contralateral controls (Fig. 1I-K).
93 Stiffness was evaluated by computing the local force-deflection curve, with an increased slope
94 indicating a stiffer tissue. At the highest fluence level (1 J/cm^2), we observed the largest increase
95 in tissue stiffness (Fig. 1L), while no difference in mechanical properties was observed between
96 RB- and non-RB-treated lobes in the absence of light (Fig. 1L). Importantly, these
97 microindentation results were consistent with the increase in stiffness observed among
98 photocrosslinked 3D collagen gels upon treatment with RB (Supplementary Fig. 3). Taken
99 together, these data suggest that RB-mediated photocrosslinking can locally alter the mechanical
100 properties of the developing pulmonary mesenchyme and suppress the formation of FGF-10-
101 induced buds.
102
103 **Treatment with RB does not adversely affect the patterns of proliferation and apoptosis**
104 **associated with epithelial budding**
105 Previous work has shown that the formation of FGF-10-induced supernumerary buds is
106 associated within an increase in epithelial proliferation[37]. To confirm that decreased budding in
107 RB-treated lungs was not accompanied by lower levels of proliferation, we quantified patterns of
108 EdU incorporation along the airway epithelium of both photocrosslinked and non-
109 photocrosslinked lung explants (Fig. 2A-C). We did not observe a significant reduction in the
110 number of EdU-positive nuclei following irradiation with green light nor upon treatment with RB
111 (Fig. 2D). In fact, at the highest fluence level (1 J/cm^2), in which we observed a decrease in FGF-
112 10-induced budding (Fig. 1), we observed a modest increase in epithelial proliferation (Fig. 2D);
113 however, the increased stiffness associated with this treatment condition was sufficient to inhibit
114 the formation of any supernumerary buds (Fig. 1E, 2C-D).
115

116 Previous work has suggested that RB-mediated crosslinking in the cornea can be associated with
117 increased cell death at high fluence levels[17]. To determine if decreased epithelial budding in RB-
118 treated lungs was associated with a change in apoptosis, we stained cultured explants for CC3
119 immunofluorescence. Neither irradiation with green light nor treatment with RB appeared to cause
120 any qualitative changes in cell apoptosis. We did not observe elevated levels of CC3-positive
121 nuclei within the airway epithelium of ectopically stiffened lungs, as compared to either "no light"
122 or contralateral controls (Fig. 3A-B, Supplementary Fig. 4A-D). However, as a positive control,
123 explants cultured in the presence of staurosporine, a pharmacological activator of apoptosis,
124 elicited increased numbers of CC3-positive nuclei within all treatment conditions (Fig. 3C-D,
125 Supplementary Fig. 4E-G). Thus, neither decreased proliferation nor increased apoptosis appear
126 to be associated with the changes in FGF-10-induced bud formation that follow RB-mediated
127 photocrosslinking.
128

129 **Computational model of FGF-10-induced budding morphogenesis suggests that increased**
130 **mesenchymal stiffness can suppress epithelial buckling**

131 To determine how tissue stiffness influences FGF-10-driven budding morphogenesis, we created
132 a computational model of the embryonic airway and surrounding pulmonary mesenchyme that
133 combined morphogen diffusion and continuum mechanics (Fig. 4). As a first approximation, the
134 airway epithelium was modeled as a thin layer of tissue overlying a thick mesenchyme containing
135 a single focal source of FGF-10 (Fig. 4A, Supplementary Fig. 5). As described previously[39], tissue
136 growth was modeled by decomposing the overall deformation of the tissue ($\boldsymbol{F}$) into a component
137 due to elastic deformation ($\boldsymbol{F}^*$) and a component due to growth ($\boldsymbol{G}$), where $\boldsymbol{F} = \boldsymbol{F}^* \cdot \boldsymbol{G}$ and growth
138 is specified via the components of the growth tensor $\boldsymbol{G}$. FGF-10 was allowed to diffuse from this
139 focal source, and the amount of growth within the epithelium (i.e., the components of $\boldsymbol{G}$) were
140 dependent upon the local concentration of FGF-10, as governed by the growth law

141 $\dot{G}_x/G_x = \alpha[FGF10]$, where α represents a growth constant, G_x is the longitudinal component of $\boldsymbol{G}$,
142 $[FGF10]$ is the concentration of FGF-10, and $\{\dot{}\}$ denotes differentiation with respect to time (Fig.
143 4A, Supplementary Fig. 5). (Additional model details are provided in the Methods.) In addition,
144 since previous studies have suggested a difference in mechanical properties between
145 mesenchymal and epithelial tissues[40,41], as a first approximation, we assumed the shear modulus
146 of the mesenchyme (C_m) was smaller than that of the epithelium (C_e), and the normalized
147 mesenchymal shear modulus $\bar{C}_m = C_m/C_e < 1$. At the beginning of the simulation, no growth was
148 present within either the epithelium or mesenchyme ($G_x = 1$) (Fig. 4B). However, as time
149 progressed, FGF-10 diffusion promoted longitudinal growth within the epithelium that caused this
150 layer to buckle and create multiple bud-like structures, which formed simultaneously (Fig. 4B,
151 Supplementary Movies 1 and 2) in a manner similar to that observed in cultured embryonic
152 lungs[37]. Before buckling, compressive longitudinal stresses developed within the epithelium as G_x
153 increased, since epithelial expansion was being constrained by the adjacent layer of mesenchyme
154 (Fig. 4B). Once the FGF-10-induced buds had formed, however, the distribution of stresses
155 through the thickness of the epithelium was consistent with bending (i.e., compressive and tensile
156 stresses located along concave and convex regions of the epithelium, respectively)[42].
157
158 In previous experiments, we observed robust FGF-10-induced bud formation even if the distance
159 between the airway epithelium and the focal source of FGF-10 was varied[37]. To determine how
160 bead placement influences epithelial buckling, we varied the location of FGF-10-loaded bead in
161 our model and assessed its influence on budding morphogenesis (Fig. 4C). Although changes in
162 bead location produced subtle differences in the amplitude of the epithelial folds, we still observed
163 robust buckling in all cases, with FGF-10-induced buds exhibiting the same (normalized)
164 characteristic wavelength $(\bar{\lambda})$, as seen experimentally[37] (Fig. 4C-D). In addition, each simulation

165 predicted the onset of buckling at the same critical axial load (P_{cr}), which plateaued following the
166 formation of new epithelial buds (Fig. 4E)[42]. Systematic analysis of other model parameters, such
167 as the magnitude of the negligible transverse point force (Supplementary Fig. 6), the mesh size
168 (Supplementary Fig. 7), the growth constant (α) (Supplementary Fig. 8), the nondimensional
169 FGF-10 localization constant ($\overline{k}$) (Supplementary Fig. 9), as well as the overall size of the model
170 domain (Supplementary Fig. 10), did not substantially alter the predicted patterns of FGF-10-
171 induced buckling morphogenesis.
172
173 We then used our computational model to determine whether increased mesenchymal stiffness
174 was sufficient suppress the formation of epithelial buds in response to a focal source of FGF-10
175 (Fig. 5A-B). Indeed, consistent with our photocrosslinking experiments, simulations with larger
176 mesenchymal shear moduli (e.g., $\overline{C_m} = 0.5, 1$) did not produce any FGF-10-induced epithelial
177 buds, despite similar levels of growth (G_x) within the airway epithelium (Fig. 5C-D, Supplementary
178 Movies 3-4). In these cases, epithelial growth did not produce compressive stresses sufficient to
179 cause buckling (Fig. 5D). Instead, the magnitude of the computed stresses increased
180 monotonically without exceeding P_{cr} (Fig. 5D). Taken together, these computational results
181 suggest that RB-mediated photocrosslinking can be used to modulate the mechanical properties
182 of embryonic organs and influence epithelial patterning and morphogenesis.

183 **Discussion**

184 Several decades worth of experiments have investigated the mechanical properties of developing
185 tissues [3–6,43]. During that time, multiple studies have shown that time-dependent changes in tissue
186 stiffness are associated with numerous developmental processes, such as gastrulation[3], egg
187 cleavage[5], elongation[4], and invagination[6]. More recently, this work has begun to investigate how
188 differences (or gradients) in mechanical properties might influence patterns of differentiation
189 during development[43–48]. However, these efforts have often used *in vitro* techniques with either
190 isolated progenitor cells[49,50] or organoid cultures[12–14] to investigate the effect of ECM stiffness. As
191 a result, to date, this idea has not been tested directly *in vivo*, in part owing to a lack of
192 experimental techniques to perturb tissue stiffness within intact embryonic organs.

193

194 Here, we used RB-mediated photocrosslinking to locally modulate the mechanical properties of
195 the pulmonary mesenchyme in cultured embryonic lungs. Photo-induced changes in tissue
196 stiffness impacted whether or not epithelial buds formed in response to FGF-10. Importantly,
197 treatment with RB did not negatively affect the patterns of cell proliferation and apoptosis
198 associated with budding morphogenesis . Instead, increased mesenchymal stiffness suppressed
199 epithelial buckling and FGF-10-induced budding events. Consistently, a computational model of
200 the embryonic airway and surrounding pulmonary mesenchyme indicated that changes in
201 mechanical properties within developing organs can profoundly influence epithelial
202 morphogenesis and patterning.

203

204 Photoactivatable molecules have been previously to modulate the stiffness of optically accessible
205 adult tissues, such as the cornea and skin[18–21]; however, our current study is the first to employ
206 this technique to alter the mechanical properties within a developing embryonic organ. We
207 capitalized on the capability of RB to covalently crosslink the ECM, particularly collagen fibrils[19].

208 In a simplified collagen gel system, significant RB-induced crosslinking was demonstrated
209 previously using scanning electron microscopy (SEM) and produced an increase in the apparent
210 stiffness of the collagen network [15], similar to the results included above (Supplementary Fig. 3).
211 The protein-protein crosslinking caused by RB is often attributed to the production of singlet
212 oxygen via energy transfer (type II reaction)[21]; however, molecular dynamics simulations and
213 experimental data have also suggested that RB crosslinking in low oxygen settings might favor
214 electron transfer (type I reaction) with positively-charged amino acids, such as arginine and
215 lysine[16,51]. Consistent with this idea, RB crosslinking within the rabbit cornea was enhanced using
216 arginine in an oxygen-free setting and resulted in an increased Young's modulus as compared to
217 controls[52]. Still, the exact mechanism by which activated RB produces protein-protein crosslinks
218 is unclear and remains an area of active investigation. Regardless, the extent of RB-mediated
219 crosslinking can be tuned by varying the irradiance and fluence of the activating light[19], and these
220 values must be carefully selected depending on the application and desired result. For instance,
221 the ability of photosensitizers like RB to degrade ECM and cause cell death is commonly used
222 during photodynamic therapy (PDT) to improve cancer treatment[53,54]. Here, to modify the
223 mechanical properties of developing tissues, RB is particularly advantageous owing to its
224 activation with green, as opposed to ultraviolet (UV) light, which is needed for riboflavin-mediated
225 crosslinking but is more phototoxic[19]. Even so, photocrosslinking requires the tissue to be optically
226 accessible, and this could limit its *in vivo* use within certain animal models, such as developing
227 mouse embryos. In such instances, *ex vivo* organ culture could be combined with RB-mediated
228 photocrosslinking, as well as genetic modulation of various ECM crosslinking enzymes, such as
229 lysyl oxidase (LOX), or LOX-like-mediated remodeling[55] and non-enzymatic collagen glycation[56],
230 to modulate tissue stiffness *in vivo*.
231

232 Here, we showed that local changes in stiffness can modulate FGF-10-induced buckling
233 morphogenesis, and these data indicate that regional differences in mechanical properties can
234 influence epithelial folding events, which involve a physical instability, such as gut villification,
235 intestinal looping, cortical folding of the brain, crypt formation within the small intestine, and tooth
236 invagination[12,13,38,57–61]. Although previous experiments using isolated airway epithelial explants in
237 3D gels of reconstituted basement membrane protein showed that branch formation and spacing
238 was unaffected by differences in gel stiffness[29], here we found that increased mesenchymal
239 stiffness can suppress FGF-10-induced budding within intact embryonic lungs. During normal
240 lung development, new lateral branches emerge along the length of the primary bronchus in a
241 proximodistal fashion[25]; however, it is unclear if spatiotemporal patterns of tissue stiffness
242 influence these branching dynamics. Still, ECM patterning has been implicated in the
243 morphogenesis of new airways in the embryonic lung[41], and similar mechanisms are thought to
244 contribute to kidney[62], mammary gland[10], and salivary gland development[9]. FGF-10 expression is
245 also an important regulator airway branching morphogenesis[36], but our data suggest that focal
246 sources of FGF-10 are not the sole determinant of the overall branching pattern. Although
247 computational modeling has been used to predict patterns of FGF-10 expression[63], these
248 simulations have not yet incorporated explicitly the role of tissue mechanics. Our
249 photocrosslinking experiments emphasize the importance of biophysical factors during airway
250 branching morphogenesis[27,29,30,32,33,41], as well as the interplay between growth factor signaling
251 and mechanical forces[33,35,64].
252
253 We also believe that RB-mediated photocrosslinking can be incorporated into dynamic studies of
254 organ morphogenesis. For instance, the mechanism of formation for tissues that appear to
255 undergo a physical instability, such as buckling, folding, bending, or looping[12,13,38,57–61] can be
256 further validated using RB photocrosslinking. Further, we propose this technique, which only

257 impacts the mechanical properties of the ECM, can be used to parse the hypothesized
258 mechanical inputs that either smooth muscle cells or the ECM provide to sculpt the
259 morphogenesis of a variety of branched epithelial networks[9,10,41,62,65,66]. Although here we focused
260 on epithelial buckling, a similar approach can be used to investigate the role of tissue mechanics
261 in cell differentiation. Spatial differences in both gene expression encoding for an ECM-modifying
262 enzyme as well as cells involved in maintenance of the microenvironment have been observed
263 within the developing kidney[62], suggesting differences in matrix stiffness may direct
264 organogenesis. A combination of novel techniques to modulate tissue stiffness, such as RB
265 photocrosslinking, and methods to measure *in vivo* mechanical properties will lead to an overall
266 greater understanding of how biophysical cues direct morphogenesis and development.

267 **Methods**

268 Ex Vivo Culture of Embryonic Lungs

269 Fertilized White Leghorn chicken eggs were incubated in a humidified forced-draft incubator at
270 37°C until HH stage 26[67]. Fine forceps were used to dissect embryonic lungs under a
271 stereomicroscope (SZX7, Olympus; Waltham, MA) in PBS supplemented with antibiotics (50 U/ml
272 penicillin/streptomycin, Invitrogen; Carlsbad, CA). Embryonic lung explants were then cultured at
273 the fluid-air interface for 24 hr at 37°C on Nucleopore membranes (25 mm-diameter, pore size: 8
274 µm) in DMEM/F12 medium (without HEPES) that had been supplemented with 5% fetal bovine
275 serum (FBS, heat inactivated) and antibiotics (50 U/ml penicillin/streptomycin)[68]. To elicit FGF-
276 10-induced supernumerary buds, agarose beads (100-200 mesh Affi-Gel Blue Media, Bio Rad;
277 Hercules, CA) containing exogeneous FGF-10 (345-FG, R&D Systems; Minneapolis, MN) were
278 implanted within the pulmonary mesenchyme along regions of the primary bronchus that do not
279 normally branch, as previously described[37]. In some experiments, the culture medium was
280 supplemented with 1 μM staurosporine (9953S, Cell Signaling; Danvers, MA) to induce cell
281 apoptosis[27]. Bright-field images of cultured lung explants were captured at 0, 3, and 24 hr using
282 a Zeiss AxioVert microscope equipped with a 5×, NA 0.15, LD A-Plan objective (Zeiss;
283 Oberkochen, Germany).

284

285 Photocrosslinking using Rose Bengal

286 RB was delivered to the embryonic lungs by introducing RB-soaked agarose beads, similar to the
287 technique used to introduce growth-factor loaded beads as previously described[37]. Briefly, small
288 agarose beads approximately 75-150 µm in diameter (100-200 mesh Affi-Gel Blue Media, Bio
289 Rad; Hercules, CA) were rinsed overnight in PBS at 4°C and then allowed to soak in droplets of
290 either 100 µg/mL recombinant human FGF-10 (345-FG, R&D Systems; Minneapolis, MN) in PBS
291 or 100 µg/mL RB (330000, Sigma; St. Louis, MO) in DI water + 100 µg/mL rhFGF-10 in PBS for

292 2-3 hr at room temperature. Using a pair of fine forceps, small incisions were made within the
293 pulmonary mesenchyme near the ventral epithelium and a single bead was placed within. The
294 explants were then cultured for 3 hr at 37°C, as described above, to allow the RB to diffuse from
295 the bead into the surrounding tissue. Afterwards, a subset of lungs were then exposed to 555 nm
296 light (BioLambda; São Paulo, Brazil) to deliver an irradiance of 25 mW/cm^2 and fluence of either
297 0.1 J/cm^2, 0.5 J/cm^2, 1 J/cm^2, 2 J/cm^2, 5 J/cm^2, or 10 J/cm^2 (control lungs were not exposed, as
298 indicated by "no light"). After irradiation, lungs were then allowed to culture for the remainder of
299 the 24 hr.
300
301 Immunofluorescent staining and imaging
302 Cultured explants were fixed in 4% paraformaldehyde in PBS for 15 minutes, permeabilized and
303 blocked using a solution of 10% goat serum and 0.3% Triton X-100 in PBS (PBST) for 1 hr at
304 room temperature. To detect proliferating cells in S-phase, the Click-iT EdU Imaging Kit
305 (Invitrogen; Carlsbad, CA) was used (explants were pulsed with EdU for 20 minutes preceding
306 fixation). Samples were then incubated with primary antibody overnight on a shaker in 4°C. The
307 following primary antibodies were used: anti-LCAM (1:100 dilution, 7D6, Developmental Studies
308 Hybridoma Bank; Iowa City, IA) and anti-cleaved caspase-3 (Asp175) (1:200 dilution, 9661, Cell
309 Signaling; Danvers, MA). Samples were washed six times for 1 hr using PBS, and then incubated
310 with Alexa Fluor-conjugated secondary antibody overnight on a shaker in 4°C (1:200 dilution,
311 Invitrogen; Carlsbad, CA). Stained explants were dehydrated in a graded methanol series and
312 optically cleared using Murray's clear. Whole-mount samples were then imaged using a Zeiss
313 LSM 800 laser scanning confocal microscope with a 20×, NA 0.8, Plan-Apochromat objective
314 (Zeiss; Oberkochen, Germany).
315
316

317 Micromechanical testing of embryonic lung explants

318 Cultured explants underwent unconfined-compression testing using an ~70 μm cylindrical
319 fabricated microindenter with a Microsquisher (MT G2, CellScale; Waterloo, ON, Canada) to
320 determine differences in tissue stiffness, similar to previously described[69]. The pulmonary
321 mesenchyme of cultured explants was compressed using the cylindrical microindenter in a region
322 of the mesenchyme near the implanted bead on each lobe. The compression test settings within
323 the SquisherJoy software (Version 5.23, CellScale; Waterloo, ON, Canada) specified a total
324 displacement of 500 μm over a 30s ramp. The indenter tip was positioned ~380 μm above the top
325 of the sample, resulting in samples undergoing ~120 μm of displacement (exact tissue
326 displacement was calculated in post-processing, as described below). Samples were tested a
327 minimum of two times, and the axial force and total displacement were tracked by the front-
328 camera and SquisherJoy software (Supplementary Fig. 2). The resulting force vs time curves
329 were plotted and used to determine the time of contact (t_c) (Supplementary Fig. 2)[69]. These
330 curves were used to determine the tissue deflection (δ_T) and the resulting force vs tissue
331 deflection curves were plotted for each test (Supplementary Fig. 2)[69]. The two replicate curves
332 were averaged for each sample, and sample curves were averaged across their respective
333 treatment group to create the overall force vs tissue deflection curves (Fig. 1). Stiffness values
334 were calculated by fitting a nonlinear curve[7] to each individual lung's force vs tissue deflection
335 curve using Matlab (Version R2018A; Natick, MA) to obtain four free parameters. The tissue
336 stiffness was then calculated as a function of tissue deflection and these parameters[7] and
337 averaged across treatment group to obtain a mean stiffness value and standard deviation. The
338 stiffness value obtained at a tissue deflection of 60 μm was selected for comparison between
339 groups (Fig. 1).

340

341

342 Collagen Gel Preparation and Mechanical Testing

343 Collagen solutions were obtained by mixing acid-solubilized rat tail collagen I (354249, Corning;
344 Corning, NY) with an equal volume of a neutralizing buffer (100mM HEPES solution in 2x PBS,
345 at pH 7.3)[70]. The final concentration of collagen was adjusted to 4 mg/mL by adding adequate
346 volumes of neutralized collagen solution and ice cold 1x PBS. This mixture was aliquoted into
347 cylindrical PDMS molds with a diameter of 5mm and a height of 2mm, and then allowed to
348 polymerize for 1 hour at 37°C. To achieve cross-linking, the plugs of polymerized collagen were
349 extracted from their molds and immersed in a 100 μg/mL solution of RB for 24 hr, and then
350 exposed to a 555 nm laser source with an irradiance of 25 mW/cm^2 and a fluence of 0.5 J/cm^2
351 (BioLambda; São Paulo, Brazil). The macroscopic properties of cylindrical collagen plugs were
352 estimated using a microscale compression system (Cell Scale; Waterloo, ON, Canada). Using
353 established protocols[71], collagen gels were subjected to uniaxial unconfined compression testing
354 by means of a 6mm x 6mm platen fixed to a microbeam of known length (57 mm), diameter
355 (0.4064 mm) and elastic modulus (411 GPa). Five stress relaxation steps were imposed by
356 applying a deformation equal to 2% of the unloaded gel height, followed by a 3-minute hold phase.
357 In virtue of the nearly linear responses observed at equilibrium, the bulk mechanical behavior
358 measured under unconfined compression was modeled using a compressible neo-Hookean
359 strain energy density function:

360 $$W = \frac{c}{2}(\bar{I}_C - 3) + \frac{1}{D}(J-1)^2$$

361 The material stiffness of the photocrosslinked collagen networks was reported as the neo-
362 Hookean shear modulus c [72].

363

364

365

366 Computational Modeling

367 A nonlinear computational model of the embryonic airway was created in COMSOL Multiphysics
368 (Version 5.5; Burlington, MA). The epithelium was modeled as a growing layer supported by a
369 foundation of mesenchyme. The modeled lung was assumed to behave as a hyperelastic material
370 with a Blatz-Ko strain-energy density function, W:

371 $$W = C_i\left[\boldsymbol{I_1^*} + \frac{1-2\nu}{\nu}\left(\boldsymbol{J}^{*\left(-2\boldsymbol{\nu}/1-2\boldsymbol{\nu}\right)} - 1\right)\right]$$

372 where C_i is the shear modulus of either the epithelium or the mesenchyme, $\boldsymbol{I_1^*}$ is the first elastic
373 strain invariant, ν is Poisson's ratio, and $\boldsymbol{J}^*$ is the elastic volume ratio. The shear modulus of the
374 epithelium (C_e) was set to equal 1 while the mesenchyme (C_m) was set to 0.1 (except in the
375 increased stiffness perturbation, as noted below). Poisson's ratio (ν) was set to 0.49 for the entire
376 model, making it nearly incompressible.

377

378 Growth was included by decomposing the overall deformation gradient tensor $\boldsymbol{F}$ into a component
379 due to growth ($\boldsymbol{G}$) and a component due to elastic deformation ($\boldsymbol{F}^*$) via $\boldsymbol{F} = \boldsymbol{F}^* \cdot \boldsymbol{G}$ [73]. Longitudinal
380 growth was included in the epithelium where the growth in the x-direction, $\boldsymbol{G_x}$, was described by:

381 $$\frac{\dot{\boldsymbol{G}}_{\boldsymbol{x}}}{\boldsymbol{G_x}} = \alpha[FGF10]$$

382 where α is a defined growth constant and $[FGF10]$ is the concentration of modeled growth factor.
383 The modeled mesenchyme was given a no growth condition. The Cauchy stress tensor, $\boldsymbol{\sigma}$,
384 depends only on the elastic deformations and was given by:

385 $$\boldsymbol{\sigma} = \boldsymbol{F}^* \cdot \frac{\partial \boldsymbol{W}}{\partial \boldsymbol{F}^{*\boldsymbol{T}}}$$

386 We report the non-dimensionalized Cauchy stress in the x-direction, $\overline{\sigma_x}$, given by $\overline{\sigma_x} = {}^{\sigma_x}/_{C_e}$. The
387 edge of the modeled bead was given the initial condition of $[FGF10] = 1$ while the outer edge of
388 the mesenchyme was given the boundary condition of $[FGF10] = 0$, to recapitulate the media sink

389 (Supplementary Fig. 5). The outer edge (luminal/apical surface) of the epithelium had a zero flux
390 condition, mimicking the barrier function it performs (Supplementary Fig. 5). Diffusion of the
391 modeled growth factor was assumed to follow Fick's Second Law of Diffusion. We assumed one-
392 dimensional, steady-state diffusion, which simplifies to the following:

393 $$\frac{\partial^2[FGF10]}{\partial x^2} - \overline{k}[FGF10] = 0$$

394 where $\overline{k}$ is the non-dimensionalized localization parameter given by $\overline{k} = {}^{k}/_{D_i}$. Both diffusion
395 constants for the epithelium (D_e) and mesenchyme (D_m) were set to equal 1. The non-
396 dimensionalized localization parameter ($\overline{k}$) was set to equal 1 in the core model (unless otherwise
397 noted in the varying localization parameter models). Additionally, to reduce the computational
398 load and computing time, the geometry was halved symmetrically along the y-axis midline and
399 results were mirrored. A small positive point force in the y-direction was added in the middle of
400 the epithelium to disrupt equilibrium. Except for the outer edge of the epithelial layer in the x-
401 direction, all other outer edges were constrained using rollers (Supplementary Fig. 5).
402
403 The model underwent various perturbations to test its robustness as well as the biophysical
404 mechanisms from experimental data, including varying $\alpha, \overline{k}, \overline{F_p}$ as well as the location of the growth
405 factor source, mesh size, and domain size (Supplementary Fig. 6-10). The photoactivatable
406 crosslinking and tissue stiffening induced by RB treatment was recapitulated in the model by
407 increasing the shear modulus of the mesenchyme while keeping all other aspects the same.
408
409 <u>Statistics</u>
410 Data represent means ± standard deviation for at least three independent experiments. Statistical
411 comparisons were made using either a Student's t-test, or a one- or two-way ANOVA, followed
412 by a Tukey post-hoc test, with p-values as specified in the figure legends.

References

1. Taber, L. A. *Biomechanics of growth, remodeling, and morphogenesis*. vol. 48 (1995).

2. Handorf, A. M., Zhou, Y., Halanski, M. A. & Li, W.-J. Tissue stiffness dictates development, homeostasis, and disease progression. *Organogenesis* **11**, 1–15 (2015).

3. Waddington, C. H. Order of magnitude of morphogenetic forces. *Nature* **144**, 637–637 (1939).

4. Adams, D. S., Keller, R. & Koehl, M. A. R. The mechanics of notochord elongation, straightening and stiffening in the embryo of Xenopus laevis. *Development* **110**, 115–130 (1990).

5. Hiramoto, Y. Mechanical properties of sea urchin eggs II. Changes in mechanical properties from fertilization to cleavage. *Exp. Cell Res.* **32**, 76–89 (1963).

6. Davidson, L. A., Oster, G. F., Keller, R. E. & Koehl, M. A. R. Measurements of mechanical properties of the blastula wall reveal which hypothesized mechanisms of primary invagination are physically plausible in the sea urchin Strongylocentrotus purpuratus. *Dev. Biol.* **209**, 221–238 (1999).

7. Zamir, E. A., Srinivasan, V., Perucchio, R. & Taber, L. A. Mechanical asymmetry in the embryonic chick heart during looping. *Ann. Biomed. Eng.* **31**, 1327–1336 (2003).

8. Lv, H. *et al.* Mechanism of regulation of stem cell differentiation by matrix stiffness. *Stem Cell Res. Ther.* **6**, 103 (2015).

9. Wang, S., Matsumoto, K., Lish, S. R., Cartagena-Rivera, A. X. & Yamada, K. M. Budding epithelial morphogenesis driven by cell-matrix versus cell-cell adhesion. *Cell* (2021).

10. Nerger, B. A. *et al.* Local accumulation of extracellular matrix regulates global morphogenetic patterning in the developing mammary gland. *Curr. Biol.* **31**, 1903-1917 (2021).

11. Baptista, M. S., Cadet, J., Greer, A. & Thomas, A. H. Photosensitization reactions of biomolecules: definition, targets and mechanisms. *Photochem. Photobiol.* **97**, 1456–1483 (2021).

12. Yavitt, F. M. *et al.* In situ modulation of intestinal organoid epithelial curvature through photoinduced viscoelasticity directs crypt morphogenesis. *Sci. Adv.* **9**, eadd5668 (2023).

13. Hushka, E. A., Yavitt, F. M., Brown, T. E., Dempsey, P. J. & Anseth, K. S. Relaxation of extracellular matrix forces directs crypt formation and architecture in intestinal organoids. *Adv. Healthcare Mater.* **9**, 1901214 (2020).

14. Marozas, I. A., Cooper-White, J. J. & Anseth, K. S. Photo-induced viscoelasticity in cytocompatible hydrogel substrates. *New J. Phys.* **21**, 045004 (2019).

15. Chan, B. P. & So, K.-F. Photochemical crosslinking improves the physicochemical properties of collagen scaffolds. *J. Biomed. Mater. Res. A* **75A**, 689–701 (2005).

16. Alarcon, E. I. *et al.* Rose Bengal binding to collagen and tissue photobonding. *ACS Omega* **2**, 6646–6657 (2017).

17. Gallego-Muñoz, P. *et al.* Corneal Wound Repair After Rose Bengal and Green Light Crosslinking: Clinical and Histologic Study. *IOVS* **58**, 3471 (2017).

18. Spoerl, E., Huhle, M. & Seiler, T. Induction of cross-links in corneal tissue. *Exp. Eye Res.* **66**, 97–103 (1998).

19. Cherfan, D. *et al.* Collagen cross-linking using Rose Bengal and green light to increase corneal stiffness. *IOVS* **54**, 3426–3433 (2013).

20. Yang, M. *et al.* Development of graphitic carbon nitride quantum dots-based oxygen self-sufficient platforms for enhanced corneal crosslinking. *Nat. Commun.* **15**, 5508 (2024).

21. Redmond, R. W. & Kochevar, I. E. Medical applications of Rose Bengal- and Riboflavin-photosensitized protein crosslinking. *Photochem. Photobiol.* **95**, 1097–1115 (2019).

22. Neckers, D. C. Rose Bengal. *J. Photochem. Photobiol., A* **47**, 1–29 (1989).

23. Lu, P. & Werb, Z. Patterning mechanisms of branched organs. *Science* **322**, 1506–1509 (2008).

24. Affolter, M., Zeller, R. & Caussinus, E. Tissue remodelling through branching morphogenesis. *Nat. Rev. Mol. Cell Bio.* **10**, 831–842 (2009).

25. Metzger, R. J., Klein, O. D., Martin, G. R. & Krasnow, M. A. The branching programme of mouse lung development. *Nature* **453**, 745–750 (2008).

26. Morrisey, E. E. & Hogan, B. L. M. Preparing for the first breath: genetic and cellular mechanisms in lung development. *Dev. Cell* **18**, 8–23 (2010).

27. Kim, H. Y., Varner, V. D. & Nelson, C. M. Apical constriction initiates new bud formation during monopodial branching of the embryonic chicken lung. *Development* **140**, 3146–3155 (2013).

28. Varner, V. D. & Nelson, C. M. Cellular and physical mechanisms of branching morphogenesis. *Development* **141**, 2750–2759 (2014).

29. Varner, V. D., Gleghorn, J. P., Miller, E., Radisky, D. C. & Nelson, C. M. Mechanically patterning the embryonic airway epithelium. *Proc. Natl. Acad. Sci.* **112**, 9230–9235 (2015).

30. Nelson, C. M. *et al.* Microfluidic chest cavities reveal that transmural pressure controls the rate of lung development. *Development* **144**, 4328–4335 (2017).

31. Nelson, C. M. & Gleghorn, J. P. Sculpting organs: mechanical regulation of tissue development. *Annu. Rev. Biomed. Eng.* **14**, 129–54 (2012).

32. Stanton, A. E. *et al.* Negative transpulmonary pressure disrupts airway morphogenesis by suppressing Fgf10. *Front. Cell Dev. Biol.* **9**, 725785 (2021).

33. Jaslove, J. M. *et al.* Transmural pressure signals through retinoic acid to regulate lung branching. *Development* **149**, (2022).

34. Gilbert, R. M., Morgan, J. T., Marcin, E. S. & Gleghorn, J. P. Fluid Mechanics as a Driver of Tissue-Scale Mechanical Signaling in Organogenesis. *Curr. Pathobiol. Rep.* **4**, 199–208 (2016).

35. Gilbert, R. M., Schappell, L. E. & Gleghorn, J. P. Defective mesothelium and limited physical space are drivers of dysregulated lung development in a genetic model of congenital diaphragmatic hernia. *Development* **148**, (2021).

36. Jones, M. R., Chong, L. & Bellusci, S. Fgf10/Fgfr2b Signaling Orchestrates the Symphony of Molecular, Cellular, and Physical Processes Required for Harmonious Airway Branching Morphogenesis. *Front. Cell Dev. Biol.* **8**, 620667 (2021).

37. Peak, K. E., Mohr-Allen, S. R., Gleghorn, J. P. & Varner, V. D. Focal sources of FGF-10 promote the buckling morphogenesis of the embryonic airway epithelium. *Biol. Open* (2022).

38. Nelson, C. M. On buckling morphogenesis. *J. Biomech. Eng.* **138**, 021005–10 (2016).

39. Rodriguez, E. K., Hoger, A. & McCulloch, A. D. Stress-dependent finite growth in soft elastic tissues. *J. Biomechanics* **27**, 455–467 (1994).

40. Campàs, O. *et al.* Quantifying cell-generated mechanical forces within living embryonic tissues. *Nat. Methods* **11**, 183–189 (2014).

41. Spurlin, J. W. *et al.* Mesenchymal proteases and tissue fluidity remodel the extracellular matrix during airway epithelial branching in the embryonic avian lung. *Development* **146**, dev175257-13 (2019).

42. Timoshenko, S. & Goodier, J. N. *Theory of Elasticity*. (1951).

43. Shellard, A. & Mayor, R. Collective durotaxis along a self-generated stiffness gradient in vivo. *Nature* **600**, 690–694 (2021).

44. Serwane, F. *et al.* In vivo quantification of spatially varying mechanical properties in developing tissues. *Nat. Methods* **14**, 181–186 (2017).

45. Zhu, M. *et al.* Spatial mapping of tissue properties in vivo reveals a 3D stiffness gradient in the mouse limb bud. *Proc. Natl. Acad. Sci.* **117**, 4781–4791 (2020).

46. Mohagheghian, E. *et al.* Quantifying stiffness and forces of tumor colonies and embryos using a magnetic microrobot. *Sci. Robot.* **8**, eadc9800 (2023).

512 47. Schappell, L. E., Minahan, D. J. & Gleghorn, J. P. A microfluidic system to measure
513 neonatal lung compliance over late stage development as a functional measure of lung tissue
514 mechanics. *J. Biomech. Eng.* **142**, (2020).

515 48. Garcia, K. E., Stewart, W. G., Espinosa, M. G., Gleghorn, J. P. & Taber, L. A. Molecular and
516 mechanical signals determine morphogenesis of the cerebral hemispheres in the chicken
517 embryo. *Development* **146**, dev174318 (2019).

518 49. Evans, N. *et al.* Substrate stiffness affects early differentiation events in embryonic stem
519 cells. *Eur. Cells Mater.* **18**, 1–14 (2009).

520 50. Guvendiren, M. & Burdick, J. A. Stiffening hydrogels to probe short- and long-term cellular
521 responses to dynamic mechanics. *Nat. Commun.* **3**, 792 (2012).

522 51. Rosales-Rojas, R. *et al.* Self-organization dynamics of collagen-like peptides crosslinking is
523 driven by Rose-Bengal-mediated electrostatic bridges. *Pharmaceutics* **14**, 1148 (2022).

524 52. Wertheimer, C. M., Mendes, B., Pei, Q., Brandt, K. & Kochevar, I. E. Arginine as an
525 enhancer in Rose Bengal photosensitized corneal crosslinking. *Transl. Vis. Sci. Technol.* **9**, 24
526 (2020).

527 53. Dolmans, D. E. J. G. J., Fukumura, D. & Jain, R. K. Photodynamic therapy for cancer. *Nat.*
528 *Rev. Cancer* **3**, 380–387 (2003).

529 54. Jafari, R., Cramer, G. M. & Celli, J. P. Modulation of extracellular matrix rigidity via
530 Riboflavin-mediated photocrosslinking regulates invasive motility and treatment response in a
531 3D pancreatic tumor model. *Photochem. Photobiol.* **96**, 365–372 (2020).

532 55. Rubera, I. *et al.* Specific Cre/Lox Recombination in the Mouse Proximal Tubule. *J. Am. Soc.*
533 *Nephrol.* **15**, 2050–2056 (2004).

534 56. Mason, B. N., Starchenko, A., Williams, R. M., Bonassar, L. J. & Reinhart-King, C. A. Tuning
535 three-dimensional collagen matrix stiffness independently of collagen concentration modulates
536 endothelial cell behavior. *Acta Biomater.* **9**, 4635–4644 (2013).

537 57. Shyer, A. E. *et al.* Villification: How the Gut Gets Its Villi. *Science* **342**, 212–8 (2013).

538 58. Savin, T. *et al.* On the growth and form of the gut. *Nature* **476**, 57–62 (2011).

539 59. Xu, G. *et al.* Axons pull on the brain, but tension does not drive cortical folding. *J. Biomech.*
540 *Eng.* **132**, 071013–8 (2010).

541 60. Osborn, J. W. A model simulating tooth morphogenesis without morphogens. *J. Theor. Biol.*
542 **165**, 429–445 (1993).

543 61. Takigawa-Imamura, H., Morita, R., Iwaki, T., Tsuji, T. & Yoshikawa, K. Tooth germ
544 invagination from cell–cell interaction: working hypothesis on mechanical instability. *J. Theor.*
545 *Biol.* **382**, 284–291 (2015).

546 62. England, A. R. *et al.* Identification and characterization of cellular heterogeneity within the
547 developing renal interstitium. *Development* **147**, dev190108 (2020).

548 63. Iber, D. & Menshykau, D. The control of branching morphogenesis. *Open Biol.* **3**, 130088
549 (2013).

550 64. Morgan, J. T., Stewart, W. G., McKee, R. A. & Gleghorn, J. P. The mechanosensitive ion
551 channel TRPV4 is a regulator of lung development and pulmonary vasculature stabilization. *Cell*
552 *Mol. Bioeng.* **11**, 309–320 (2018).

553 65. Goodwin, K. *et al.* Patterning the embryonic pulmonary mesenchyme. *iScience* **25**, 103838
554 (2022).

555 66. Young, R. E. *et al.* Smooth muscle differentiation is essential for airway size, tracheal
556 cartilage segmentation, but dispensable for epithelial branching. *Dev. Cell* (2020).

557 67. Hamburger, V. & Hamilton, H. L. A series of normal stages in the development of the chick
558 embryo. *J. Morphol.* 49–92 (1951).

559 68. Gleghorn, J. P., Kwak, J., Pavlovich, A. L. & Nelson, C. M. Inhibitory morphogens and
560 monopodial branching of the embryonic chicken lung. *Dev. Dynam.* **241**, 852–862 (2012).

561 69. Chakraborty, S., Peak, K. E., Gleghorn, J. P., Carroll, T. J. & Varner, V. D. Quantifying
562 spatial patterns of tissue stiffness within the embryonic mouse kidney. In: Nelson, C.M. (eds)
563 *Tissue Morphogenesis. Methods Mol. Biol.*, vol 2805, 171–186 (2024).

564 70. Ferruzzi, J. *et al.* Compressive remodeling alters fluid transport properties of collagen
565 networks – implications for tumor growth. *Sci. Rep.* **9**, 17151 (2019).

566 71. Kang, W. *et al.* A novel jamming phase diagram links tumor invasion to non-equilibrium
567 phase separation. *iScience* **24**, 103252 (2021).

568 72. Holzapfel, G. A. *Nonlinear Solid Mechanics: A Continuum Approach for Engineering*. (2000).

569 73. Taber, L. A. *Continuum Modeling in Mechanobiology*. (2020).

570

571 **Acknowledgments**

572 This work was supported by grants from the National Institutes of Health

573 (R01HL145147 and R01HL133163).

574

575

Author Contributions

Conceptualization: K.E.P., V.D.V.; Formal analysis: K.E.P., P.R., A.K.; Investigation: K.E.P., P.R., A.K; Writing - original draft: K.E.P.; Writing - review & editing: K.E.P., A.K., J.P.G., G.O., J.F., V.D.V.; Supervision: G.O., J.F., V.D.V.; Project administration: V.D.V.; Funding acquisition: V.D.V.

Competing Interests

The authors declare no competing interests.

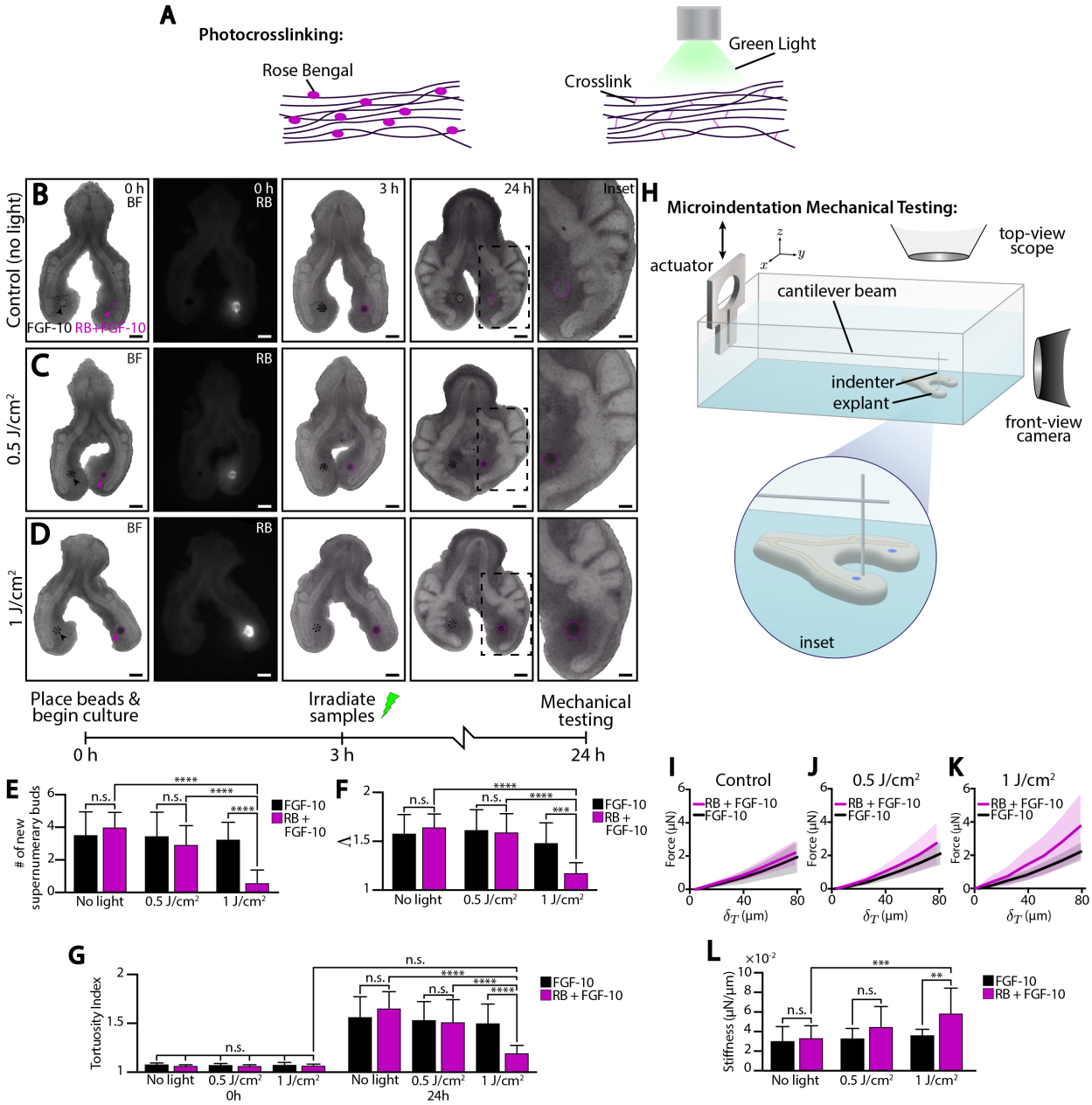

Figure 1: Photocrosslinking leads to increased tissue stiffness and inhibits FGF-10-induced epithelial buckling. (A) Schematic representation of Rose Bengal (RB), shown as magenta ovals, associating with extracellular matrix (ECM) proteins, shown as black strands. Exposure to green light leads to activation of Rose Bengal, resulting in the formation of crosslinks, shown as magenta lines, between ECM proteins. (B-D) Bright-field and fluorescent images of representative embryonic lung explants cultured ex vivo with either FGF-10 beads (left lobe, black arrow and dashed lines) or FGF-10 + RB beads (right lobe, magenta arrow and dashed lines). Fluorescent images show RB autofluorescence visualized by green light. Cultured lungs were mechanically tested at the end of 24 h. Scale bars, 200 μm. (Inset scale bars, 100 μm). (E-G) Quantification of (E) number of new supernumerary buds, (F) the epithelial contour ratio $\Lambda = L/L_0$, and (G) the tortuosity index $T = L/\overline{L}$ where L is the measured length of the ventral

epithelium at each time-point, $\overline{L}$ is the length of the straight line connecting the endpoints of L, and L_0 is the length of the ventral epithelium at t = 0 h, which is used as a reference length. A one-way ANOVA (E-F) or two-way ANOVA (G), followed by a Tukey post-hoc test, were used to make statistical comparisons. (Control, FGF-10: n = 15; Control, RB + FGF-10: n = 13; 0.5 J/cm^2, FGF-10: n = 15; 0.5 J/cm^2, RB + FGF-10: n = 15; 1 J/cm^2, FGF-10: n = 12; 1 J/cm^2, RB + FGF-10: n = 12; * $p < 0.05$, ** $p < 0.01$, *** $p < 0.001$, **** $p < 0.0001$; error bars represent s.d.). (H) Schematic representation of microindentation mechanical testing. (I-K) Averaged force versus tissue deflection (δ_T) curves for (I) control, (J) 0.5 J/cm^2, and (K) 1 J/cm^2. Curves represent the mean value while the shaded region represents standard deviation. (L) Stiffness plot for all treatment groups. A two-way ANOVA, followed by a Tukey post-hoc test, was used to make statistical comparisons. (Control, FGF-10: n = 15; Control, RB + FGF-10: n = 15; 0.5 J/cm^2, FGF-10: n = 14; 0.5 J/cm^2, RB + FGF-10: n = 13; 1 J/cm^2, FGF-10: n = 12; 1 J/cm^2, RB + FGF-10: n = 11; * $p < 0.05$, ** $p < 0.01$, *** $p < 0.001$, **** $p < 0.0001$; error bars represent s.d.).

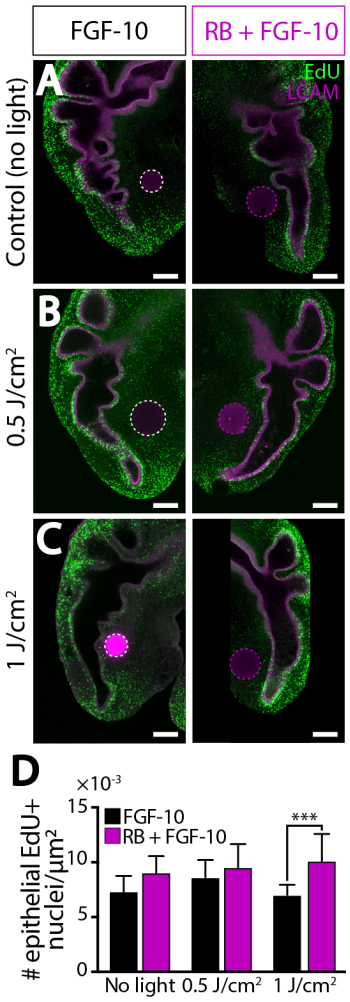

Figure 2: Photocrosslinking does not reduce rates of proliferation along the embryonic airway epithelium. (A-C) Confocal images of EdU incorporation and LCAM immunofluorescence in representative whole-mount lung explants. White or magenta dashed lines denote FGF-10 or RB + FGF-10-soaked beads, respectively. Scale bars, 200 µm. (D) Quantification of EdU incorporation within the ventral epithelium. A one-way ANOVA, followed by a Tukey post-hoc test, was used to determine significance between groups (Control, FGF-10: n = 12; Control, RB + FGF-10: n = 13; 0.5 J/cm², FGF-10: n = 13; 0.5 J/cm², RB + FGF-10: n = 12; 1 J/cm², FGF-10: n = 13; 1 J/cm², RB + FGF-10: n = 12; * $p < 0.05$, ** $p < 0.01$, *** $p < 0.001$, **** $p < 0.0001$; error bars represent s.d.).

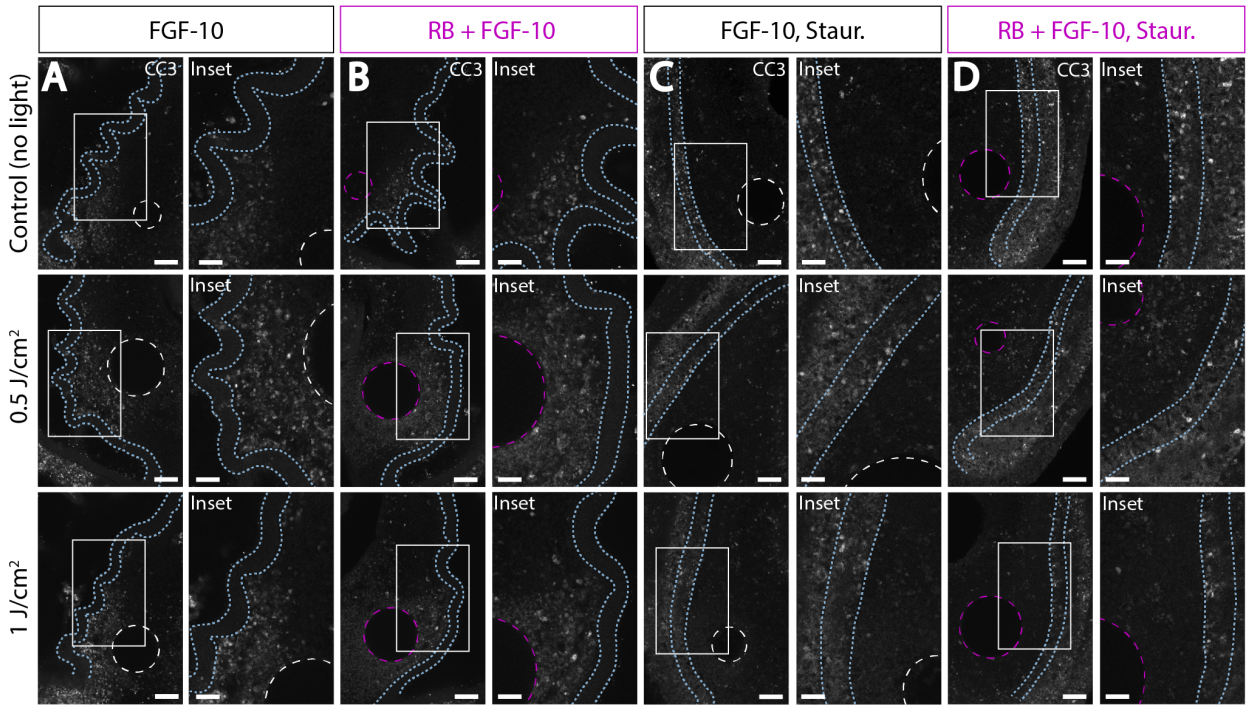

Figure 3: No apparent increase in apoptosis in photocrosslinked lung explants. (A-D) Confocal images of CC3 immunofluorescence in representative whole-mount lung explants. Some explants were treated with staurosporine (staur.), an activator of cell apoptosis (C-D). White or magenta dashed circles denote FGF-10 or RB + FGF-10-soaked beads, respectively. Blue dashed lines outline the ventral epithelium. Inset region indicated with white box. Scale bars, 100 µm. Insets scale bars, 50 µm. (Control: n = 9; 0.5 J/cm^2: n = 9; 1 J/cm^2: n = 9; Control, staurosporine: n = 9; 0.5 J/cm^2, staurosporine: n = 9; 1 J/cm^2, staurosporine: n = 9).

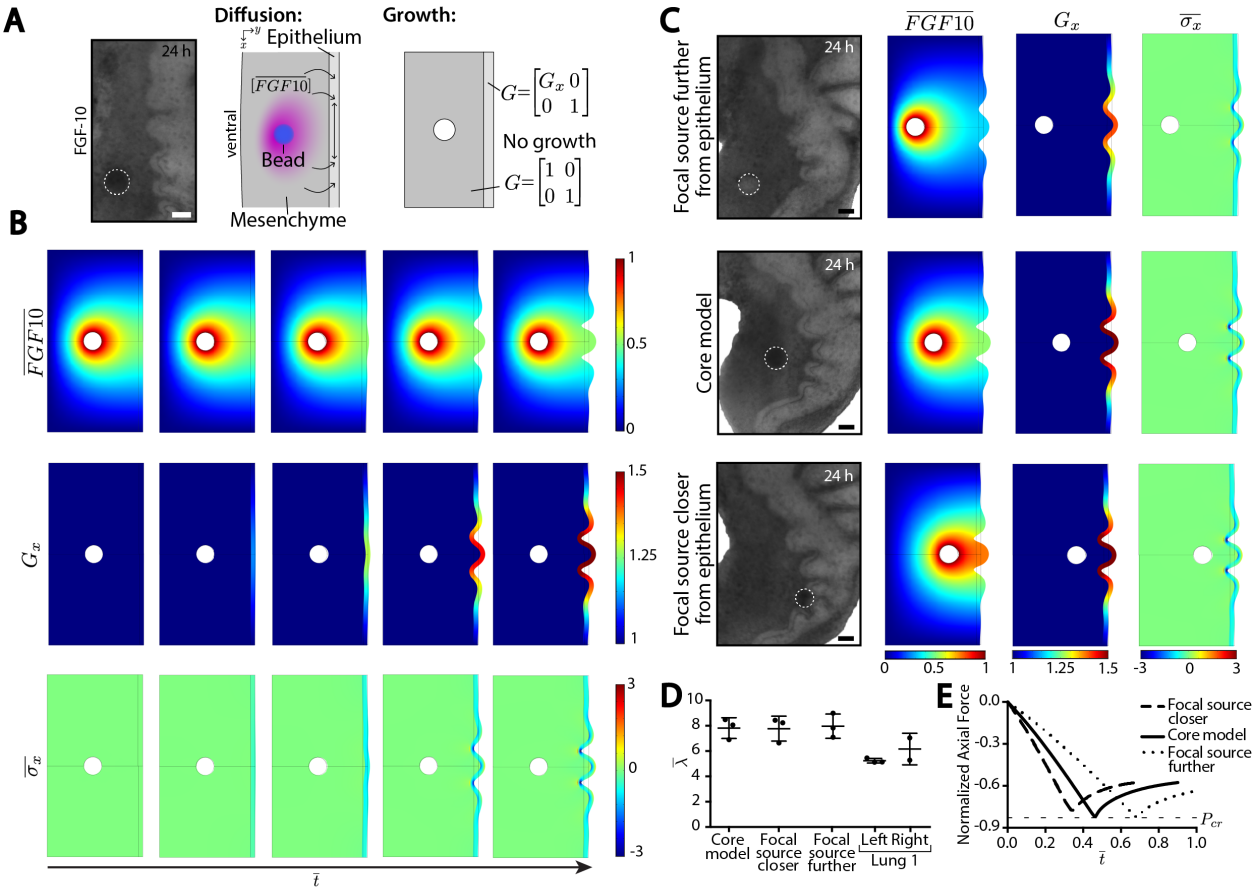

Figure 4: Computational model of FGF-10-driven buckling morphogenesis. (A) Representative bright-field image inset of an embryonic lung explant cultured with an FGF-10-loaded bead and a buckled ventral epithelium. Scale bar, 50 μm. Schematic representation of the cultured lung showing FGF-10 diffusion from the bead and stimulating the ventral epithelium to grow. Schematic representation of the computational model based on the experimental system. Growth ($\boldsymbol{G}$) within the modeled epithelial bar is specified uniaxially (G_x), but the modeled mesenchyme does not grow. (B) Core model results over non-dimensionalized time ($\bar{t}$) for normalized FGF-10 concentration ($\overline{FGF10}$), growth in the x-direction (G_x), and normalized Cauchy stress ($\overline{\sigma_x}$). (C) Varying the location of the focal source of growth factor to be further or closer to the epithelium. Representative bright-field images show an FGF-10-loaded bead at various distances from the epithelium. White dashed line indicates bead location. Scale bar = 50 μm. Results for normalized FGF-10 concentration ($\overline{FGF10}$), growth in the x-direction (G_x), and normalized Cauchy stress ($\overline{\sigma_x}$) shown at the final timepoint of the models. (D) The normalized wavelength for all three models compared to a representative lung explants shows a characteristic value. (E) Normalized axial force versus non-dimensionalized time ($\bar{t}$) for all three models. All reach a deflection point, interpreted as the critical load (P_{cr}) and denoted by the horizontal dashed line.

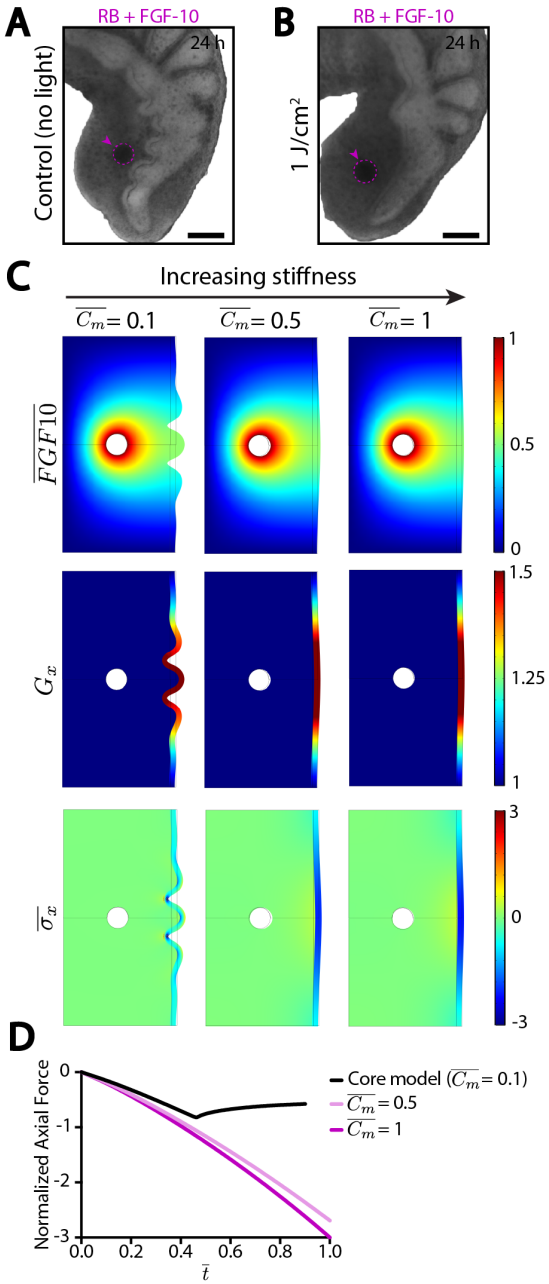

Figure 5: Computational model predicts that increased mesenchymal stiffness suppresses the formation of FGF-10-induced epithelial buds. (A-B) Representative bright-field images of (A) control or (B) 1 J/cm² (increased stiffness) lungs showing a buckled epithelium versus suppressed buckling, respectively. Magenta dashed lines indicate location of the RB+FGF-10-loaded bead. Scale bars, 100 μm (C) Computational models with increasing mesenchymal stiffness, shown as the normalized mesenchymal shear modulus $\overline{C_m}$. Results for normalized FGF-10 concentration $(\overline{FGF10})$, growth in the x-direction (G_x), and normalized Cauchy stress $(\overline{\sigma_x})$ shown at the final timepoint of the models. (D) Normalized axial force versus non-dimensionalized time $(\bar{t})$ for all three models. Only the core model reaches a deflection point, interpreted as the critical load.